International Journal of Mass Spectrometry 290 (2010) 65–71

Contents lists available at ScienceDirect

International Journal of Mass Spectrometry

journal homepage: www.elsevier.com/locate/ijms

# The relative abundances of silicon hydride clusters, $Si_nH_x^-$ ($n = 8$–$12$ and $0 \leq x \leq 25$), investigated with high-resolution time-of-flight mass spectrometry

Samuel J. Peppernick[a], K.D. Dasitha Gunaratne[b], A.W. Castleman Jr.[b,c,*]

[a] Department of Materials Science, 104 Chemistry Research Building, The Pennsylvania State University, University Park, PA 16802, USA
[b] Department of Chemistry, 104 Chemistry Research Building, The Pennsylvania State University, University Park, PA 16802, USA
[c] Department of Physics, 104 Chemistry Research Building, The Pennsylvania State University, University Park, PA 16802, USA

ARTICLE INFO

*Article history:*
Received 27 September 2009
Received in revised form
16 November 2009
Accepted 3 December 2009
Available online 16 December 2009

*Keywords:*
Silicon hydride cluster
Dusty plasma
Isotopic analysis
Reactive plasma
Time-of-flight

ABSTRACT

Results are presented of a high-resolution time-of-flight mass spectrometric study on large silicon hydride cluster anions, $Si_nH_x^-$ (where $n = 8$–$12$, $0 \leq x \leq 25$). The clusters were produced via the reactions between a dilute silane gas mixture and a laser-induced transition metal plasma. Extensive degrees of hydrogenation were observed for larger $Si_n^-$ clusters, with an onset appearing around $Si_8^-$ and continuing on into the $Si_{12}^-$ series. The relative abundances of the majority isotopes constituting a precise mass were completely analyzed allowing qualitative assessments of the stability for a particular $Si_nH_x^-$ cluster to be ascertained. The $Si_nH_x^-$ clusters are observed to possess varying abundances depending on the extent of hydrogenation and the number of silicon atoms constituting the cluster. Specific clusters, which exhibited enhanced stability in the molecular beam, are $Si_8H_6^-$, $Si_8H_8^-$, $Si_9H_5^-$, $Si_{11}H_2^-$ and $Si_{12}H_2^-$, respectively. In general, the lighter $Si_nH_x^-$ ($n = 8$–$10$) clusters were dominated by high relative abundances of the pure silicon cluster parent, $Si_{8-10}^-$, and the singly hydrogenated cluster, $Si_{8-10}H^-$. A pronounced decrease in intensity was then noted with one additional H adsorption, forming the di-hydride species, $Si_{8-10}H_2^-$. The exact converse was observed in the heavier silicon hydride series, $Si_nH_x^-$ ($n = 11$–$12$), where the pure silicon cluster parent, $Si_{11-12}^-$, and single hydrogenation species, $Si_{11-12}H^-$ are suppressed by a substantial production of an especially stable $Si_{11-12}H_2^-$ di-hydride moiety.

## 1. Introduction

A phenomenon prominently encountered in the silane ($SiH_4$) chemical vapor deposition (CVD) of amorphous silicon thin films is the creation of dusty plasmas composed of hydrogenated silicon clusters, $Si_nH_x$ [1]. Surface contamination by $Si_nH_x$ nanoparticles, formed by gas-phase nucleation processes in the deposition plasma, impedes the production of high quality films and limits growth rates [2,3]. On the other hand, silicon nanocrystals [2–6] have been shown in numerous reports to display enhanced photoluminescent properties [7–11]. The extent of the photoluminescence was observed to be dependent upon quenching dangling surface bonds of the silicon nanoparticle from passivation of atomic hydrogen [8,9]. In conjunction with mass spectrometry, small molecular clusters offer a unique arena to explore the dynamics associated with the reactive discharge of $SiH_4$ from high-energy plasmas. Such investigations could lead to a more thorough understanding of the formation mechanisms governing the production of relatively large $Si_nH_x$ nanoparticles (*e.g.*, $n > 20$) for controlled film depositions or unraveling their anomalous photoluminescent behavior.

Numerous experimental probes have been elegantly employed to elucidate the processes occurring during the formation of microparticulate powders via reactive plasmas [12–25]. Several fundamental questions persist such as charge mediation, thermophoresis and other related forces unique to plasmas, and the compositional nature of the protoparticles themselves [27]. It is these elementary protoparticles [1] or seed clusters whose presence in the plasma inherently drives the initial nucleation phase to extensive accretion of substantially large micrometer sized particulates [1–6,28]. Indeed, it has been extensively demonstrated that negative silicon hydride cluster ions, $Si_nH_x^-$, are prospective candidates for the protoparticles [12–19]. The existence of sheath fields in radio-frequency generated plasmas effectively traps negatively charged ions, allowing a stagnation time to transpire that ultimately leads to the rampant onset of plasma-mediated polymerization [13–19]. Affixing mass spectrometers downstream from the afterglow region permits detection of the products resulting from the negative ion clustering reactions. Signals covering an expansive distribution of cluster anion sizes were collected, reaching substantial masses such as $Si_{40}H_x^-$ [13–15]. On the other hand, the exact converse is observed for the detection of posi-

---

[*] Corresponding author. Tel.: +1 814 863 3413; fax: +1 814 865 5235.
*E-mail address:* awc@psu.edu (A.W. Castleman Jr.).

1387-3806/$ – see front matter © 2009 Elsevier B.V. All rights reserved.
doi:10.1016/j.ijms.2009.12.005

tively charged silicon hydride cluster aggregates [26,27]. In fact, the spontaneous agglomeration of cationic species was found to be rate-limited, hindered by sequential reactions that terminated in the formation of a $Si_4D_6^+$ complex [26]. Therefore, obtaining a comprehensive understanding of anionic $Si_nH_x^-$ cluster motifs, which have displayed propensity in molecular beams from $SiH_4$ arc discharge sources [20], may provide additional insight into the formation mechanisms governing the rudimentary plasma polymerizations [1,4,13].

While the observation of ionic silicon hydride clusters in mass spectrometers is a thoroughly documented area [12–25], only a few studies afforded sufficient mass resolution to discriminate between successive single amu separations [13,15,18–20,23]. However, even with high mass resolving powers employed in these investigations, complications still exist in definitive mass assignment, due to the three naturally occurring isotopes of elemental silicon, whose existence quickly poses a non-trivial task to deconvolute mass spectra containing multiple overlapping isotope distributions. Thus information regarding the relative abundance of any one particular $Si_nH_x^-$ cluster produced from the plasma is not obtained, which may prove critical when formulating kinetic models [4–6,29] describing the homogeneous nucleation pathways of negative $Si_nH_x^-$ cluster ions. Moreover, extracting intensity contributions and abundance data from experimental mass spectra would aid theoretical treatments in formulating reliable methodologies to calculate properties of these complicated molecular species.

We have embarked upon acquiring high-resolution time-of-flight (TOF) mass spectra for $Si_nH_x^-$ clusters, and modeled the observed intensity profiles with simulated distributions calculated from the known isotopic abundances of silicon. In principle, this method directly affords the relative abundance of any isotope of a $Si_nH_x^-$ cluster, but the results are limited here to only the most abundant $^{28}Si_nH_x^-$ species. The negative cluster ions were produced from the laser-induced reactions between $SiH_4$ and a transition metal plasma, which can be coarsely approximated as conditions occurring for the CVD of $SiH_4$ to form amorphous silicon thin films. Hence, due to the non-equilibrium conditions of the laser vaporization cluster source employed in the present experiments, the interpretation of a particular $Si_nH_x^-$ cluster's stability can only be regarded as a qualitative assessment based on the intensities deduced from the simulated $Si_nH_x^-$ isotope distributions. Nevertheless, these results bear relevance on unraveling the dynamical processes observed during radio-frequency discharges of $SiH_4$ and provide further evidence for the role small $Si_nH_x^-$ clusters ions have in determining the formation of microparticulate powders.

## 2. Experiment

The experiment was performed on a laser vaporization supersonic cluster ion source coupled to a high-resolution TOF mass spectrometer [30–33]. Pure silicon ($Si_n$) and silicon hydride clusters ($Si_nH_x$), in various charge states, are produced in the source region by delivering a pulsed jet of diluted $SiH_4$ (∼1% seeded in high purity He) over an energetic transition metal plasma. The absolute backing pressure of the reactant $SiH_4$ gas was typically 4 atm. The plasma is created by impinging the surface of a metal target with the tightly focused second harmonic output of a pulsed Nd:YAG laser beam (532 nm, 10 Hz, ∼150 mJ/pulse). The metal target is kept in continuous translation and rotation by a 1 rpm stepping motor to ensure a fresh spot with each laser pulse. The clusters formed in the laser vaporization region supersonically expand into vacuum and are collimated into a molecular beam after exiting a skimming orifice. Negatively charged clusters are perpendicularly extracted by a pulsed Wiley-McLaren electrostatic grid assembly [34] and analyzed by TOF mass spectrometry. Mass-to-charge ($m/z$) separation is accomplished in a ∼1.8 m long field free flight tube. The ultimate resolving power of the mass spectrometer is $m/\Delta m \sim 400$, and can be attenuated with the application of appropriate voltages to various ion guides and steering optics positioned immediately after the entrance to the field free region. Mass signal is detected with a microchannel plate assembly and monitored by data acquisition software (Gagescope 12100). Typical mass spectra are averaged over 500 laser shots and calibrated against the arrival times of several atomic species.

### 2.1. Isotopic distribution modeling

Presented in Fig. 1 is the mass distribution produced from the laser-induced plasma reactions of $SiH_4$. Clusters ranging in size from the diatomic to $Si_{12}^-$ are readily generated, along with a complex array of hydrogenated $Si_nH_x^-$ clusters, producing distinct intensity patterns in the mass spectrum. The TOF spectrum of Fig. 1 is similar to the $SiH_4$ arc discharge molecular beam experiments reported by Xu et al. [20,21]. However, in that study, the extent of clustering was presented as reaching only the $Si_7H_x^-$ ($m/z$ = 196 amu) series. Observed in Fig. 1, the prominence of extensive hydride saturation is much more pronounced in the vicinity of heavier $Si_n^-$ clusters, starting at $Si_8^-$ and continuing on into the $Si_{12}^-$ mass range. The intensity profiles stem from overlapping isotopic distributions of the pure $Si_n^-$ parent and the hydrogenated analogs conforming to a precise $Si_nH_x^-$ stoichiometry. The first peak appearing within a specific cluster series is uniquely assigned to the pure $Si_n^-$ parent. The subsequent intensity patterns become exceedingly convoluted due to the three naturally occurring isotopes of elemental Si: $^{28}Si$ (92.23%), $^{29}Si$ (4.67%) and $^{30}Si$ (3.10%) [35], whose isotopic distribution becomes statistically more complex upon clustering. Addition of a single H atom to a pure $Si_n^-$ cluster simply shifts this isotope pattern 1 amu higher in mass, such that the resulting intensity variation for any $Si_nH_x^-$ series, having (in some cases) a maximum hydrogen series of $x = 25$, represents a multitude of individual isotope patterns.

Assuming equal cluster population in the molecular beam, the observed intensity for a specific peak is then a sum of the individual $Si_nH_x^-$ isotopes constituting that particular $m/z$ value. Subtract-

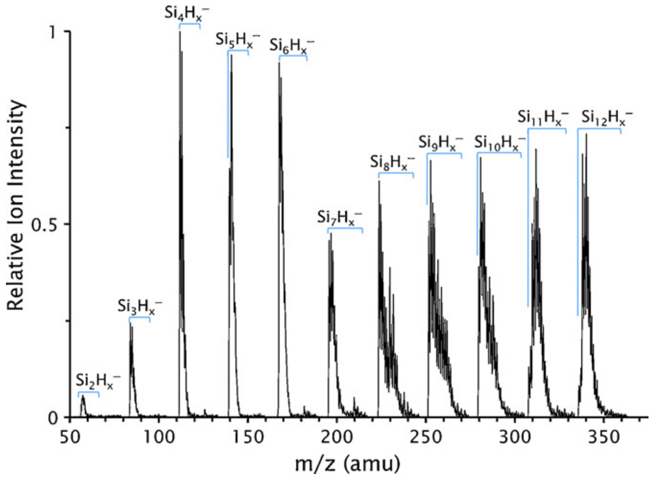

**Fig. 1.** Experimental TOF mass distribution produced from $SiH_4$ plasma reactions in the supersonic cluster ion source, displaying the regular progression of pure $Si_n^-$ and $Si_nH_x^-$ clusters with varying indexes ($x$) of H saturation. Single amu mass resolution is obtained for the entire cluster range, affording an effective resolving power of $m/\Delta m \sim 400$. From $Si_8H_x^-$ onward, intense degrees of hydrogenation become apparent, characterized by erratic intensity profiles within a specific mass window.

ing the intensity contribution of a unique stoichiometry from the experimental spectrum and normalizing the next sequential hydride cluster to the residual provides a method to deduce the fractional intensities of the degenerate $Si_nH_x^-$ isotopes. Once the relative abundances of all the masses pertaining to a $Si_nH_x^-$ cluster series have been evaluated, an isotopic envelope can then be calculated, being the final summation of the fractional intensities. This envelope should reproduce the experimental intensity profile for the analyzed $m/z$ range. In this manner, the relative abundances of the $Si_nH_x^-$ clusters present in the molecular beam can be quantified, providing clues into the local energetic stability of the parent $Si_n^-$ cluster upon successive hydrogenation.

## 3. Results and discussion

Presented in Figs. 2–6 are segmented TOF mass distributions of the $Si_8H_x^-$ ($x=0$–$21$), $Si_9H_x^-$ ($x=0$–$20$), $Si_{10}H_x^-$ ($x=0$–$25$), $Si_{11}H_x^-$ ($x=0$–$25$) and $Si_{12}H_x^-$ ($x=0$–$25$) cluster series, respectively. Black solid lines designate the experimental TOF distributions. Single amu mass resolution was achieved up to the heaviest cluster studied, corresponding to $Si_{12}H_{25}^-$. Positioned within a specific $Si_nH_x^-$ series are the calculated isotopic distributions of the pure $Si_n^-$ ($n=8$–$12$) cluster and its associated hydrogenated stoichiometries. These simulated distributions are divided into color-coded subunits, with varying hues of one distinct color interspersed across an effective ~4 amu mass range. For example, the red sector in the $Si_8H_x^-$ isotope distribution of Fig. 2 corresponds to the lightest masses, $Si_8^-$ to $Si_8H_3^-$. Conversely, the yellow portion (or orange) is delineated to the heaviest mass region, indicative of the clusters, $Si_8H_{18}^-$, $Si_8H_{20}^-$ and $Si_8H_{21}^-$, respectively. The green, blue, and violet segments signify intermediate $Si_8H_x^-$ ($4 \le x \le 16$) cluster sizes. This color-coded sequence convention is maintained in Fig. 3 through 6 for the heavier mass hydride clusters. Each simulated $Si_n^-$ and $Si_nH_x^-$ distribution is determined from the abundances of the naturally occurring isotopes of elemental silicon. The gaussian peak widths were scaled to artificially replicate the experimental mass resolution. Neglected in the analysis were isotopic mass shifts due to the presence of deuterium, $^2D$. This assumption is valid when considering the low natural abundance of $^2D$ (0.015%) in relation to the dominant $^1H$ (99.985%) isotope [35]. Subtracting the contribution of $Si_nH_{x-1}^-$ (for $n=8$–$12$ and $x=1$–$25$) from the experimental spectrum and normalizing the next sequential $Si_nH_x^-$ unit to the residual difference provided the fractional intensities of the individual distributions, as discussed above. The insets of Figs. 2–6 depict the final summed intensity envelope (solid red line) of all the isotope contributions from the pure and hydrogenated clusters tabulated in the rightmost column of the respective figures. Using this technique, the experimental intensity profile can be reproduced with a significant degree of accuracy. The fitted intensity envelope represents only those contributions from the isotopes of the indicated $Si_n^-$ and $Si_nH_x^-$ clusters. No other peak fitting or least squares routines were implemented.

Additionally, plotted in Figs. 7 and 8, are the relative abundances of the individual $Si_nH_x^-$ clusters as the number of adsorbed hydrogen atoms increases from 0 to a maximum index of $x=25$. The

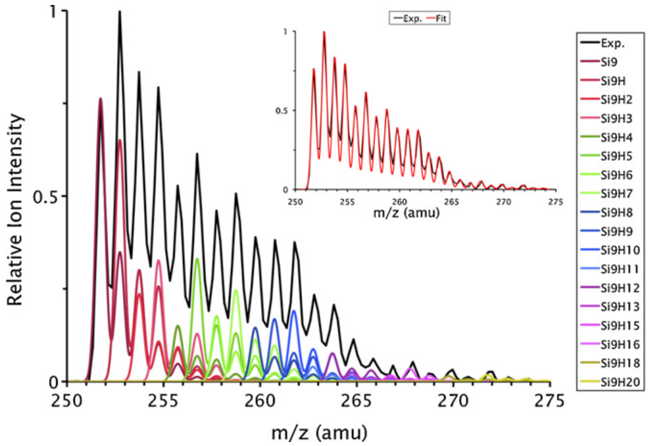

**Fig. 3.** Experimental TOF spectrum (black curve) for the $Si_9H_x^-$ mass range (252–272 amu), overlaid with the simulated isotopic distributions (red, green, blue, violet, and yellow curves) for the individual $Si_9H_x^-$ ($x=0-20$) stoichiometries. The inset displays the summed intensity envelope (red curve) of all the isotope contributions from the various $Si_9H_x^-$ clusters. Listed in the far right column are the $Si_9H_x^-$ clusters found to contribute significantly to the fitted intensity envelope. The $Si_9H_{14}^-$, $Si_9H_{17}^-$ and $Si_9H_{19}^-$ clusters were found to contribute zero relative abundance to the overall fit. (For interpretation of the references to color in this figure legend, the reader is referred to the web version of the article.)

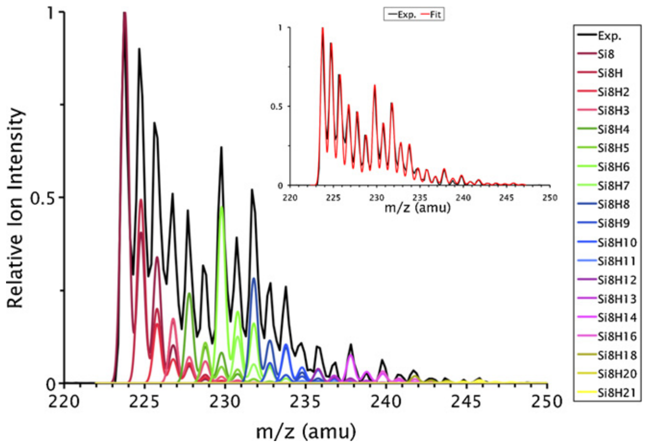

**Fig. 2.** Experimental TOF spectrum (black curve) for the $Si_8H_x^-$ mass range (224–245 amu), overlaid with the simulated isotopic distributions (red, green, blue, violet, and yellow curves) for the individual $Si_8H_x^-$ ($x=0$–$21$) stoichiometries. The method for determining the relative peak heights is described in the text. The inset displays the summed intensity envelope (red curve) of all the predicted contributions from the various $Si_8H_x^-$ isotopes. The rightmost column tabulates the clusters included in the intensity fit. The $Si_8H_{15}^-$ and $Si_8H_{17}^-$ clusters were found to contribute zero fractional intensity. (For interpretation of the references to color in this figure legend, the reader is referred to the web version of the article.)

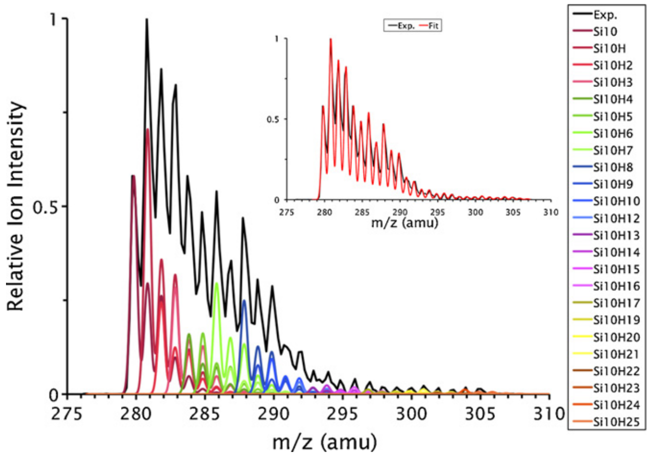

**Fig. 4.** Experimental TOF spectrum (black curve) for the $Si_{10}H_x^-$ mass range (280–305 amu), overlaid with the simulated isotopic distributions (red, green, blue, violet, yellow and orange curves) for the individual $Si_{10}H_x^-$ ($x=0-25$) stoichiometries. The inset displays the summed intensity envelope (red curve) of all the isotope contributions from the various $Si_{10}H_x^-$ clusters. The far right column lists the individual $Si_{10}H_x^-$ clusters contributing the fitted intensity envelope. The $Si_{10}H_{11}^-$ and $Si_{10}H_{18}^-$ clusters were determine to contribute zero relative abundance to the overall fit. (For interpretation of the references to color in this figure legend, the reader is referred to the web version of the article.)

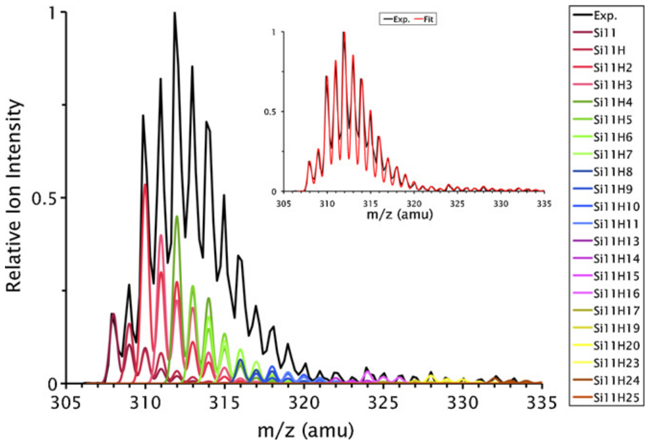

**Fig. 5.** Experimental TOF spectrum (black curve) for the $Si_{11}H_x^-$ mass range (308–333 amu), overlaid with the simulated isotopic distributions (red, green, blue, violet, yellow and orange curves) for the individual $Si_{11}H_x^-$ ($x = 0-25$) stoichiometries. Note the change in the overall intensity contour compared to lighter $Si_{8-10}H_x^-$ clusters. The inset displays the summed intensity envelope (red curve) of all the isotope contributions from the various $Si_{11}H_x^-$ clusters. The far right column lists the individual $Si_{11}H_x^-$ cluster ions contributing to the fitted intensity envelope. The $Si_{11}H_{12}^-$, $Si_{11}H_{18}^-$, $Si_{11}H_{21}^-$ and $Si_{11}H_{22}^-$ clusters were determined to contribute zero intensity to the overall fit. (For interpretation of the references to color in this figure legend, the reader is referred to the web version of the article.)

magnitude of a cluster's relative abundance plotted in Figs. 7 and 8 corresponds to the foremost $^{28}Si_nH_x^-$ isotope for that specific $m/z$ value. These charts can also be interpreted as a qualitative measurement of the stability for the various $Si_nH_x^-$ ions investigated, *i.e.*, those hydrides with a larger magnitude for the relative abundance can be considered more stable in the molecular beam. For clarity, Fig. 7 displays the relative abundances for the lighter $Si_nH_x^-$ clusters ($8 \leq n \leq 12$ and $0 \leq x \leq 10$). Shown on an expanded scale in Fig. 8, are the relative abundances of the heavily saturated $Si_nH_x^-$ clusters ($8 \leq n \leq 12$ and $10 \leq x \leq 25$). Several interesting trends regarding the effect of sequential H addition to a pure $Si_n^-$ cluster can be directly ascertained from inspection of Figs. 7 and 8.

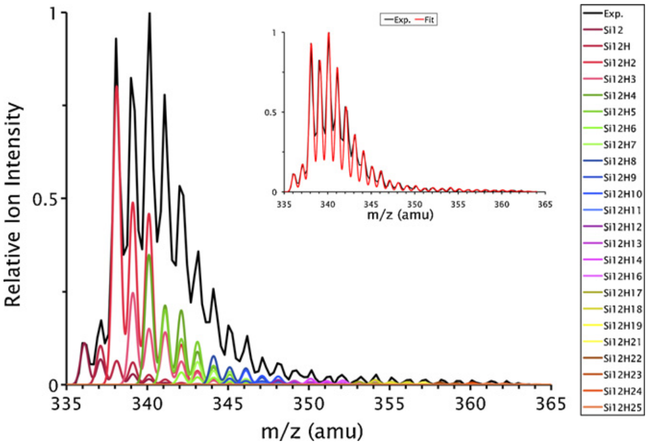

**Fig. 6.** Experimental TOF spectrum (black curve) for the $Si_{12}H_x^-$ mass range (336–361 amu), overlaid with the simulated isotopic distributions (red, green, blue, violet, yellow and orange curves) for the individual $Si_{12}H_x^-$ ($x = 0-25$) stoichiometries. Single amu mass resolution was achieved up to the heaviest hydride studied, $Si_{12}H_{25}^-$. Note the change in the overall intensity contour. The inset displays the summed intensity envelope (red curve) of all the isotope contributions from the various $Si_{12}H_x^-$ clusters. The far right column lists the individual $Si_{12}H_x^-$ cluster ions contributing to the fitted intensity envelope. The $Si_{12}H_{15}^-$ and $Si_{12}H_{20}^-$ ions were determined to contribute zero intensity to the overall fit. (For interpretation of the references to color in this figure legend, the reader is referred to the web version of the article.)

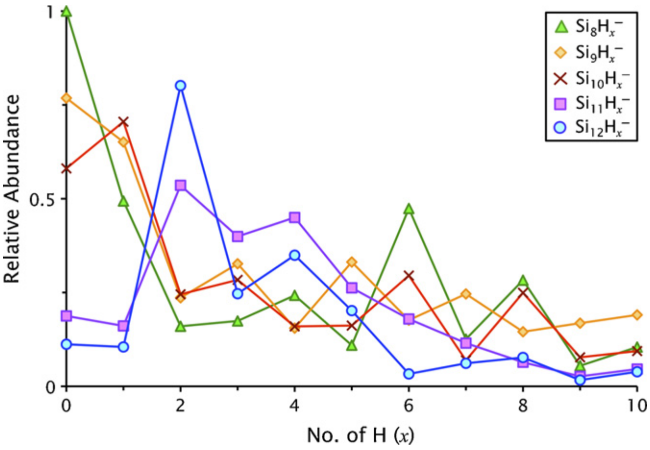

**Fig. 7.** Results of the relative abundance (*i.e.*, stability) study from the simulated isotopic distributions of the less hydrogenated $^{28}Si_nH_x^-$ ($n = 8-12$ and $x = 0-10$) anions. Each point represents the evaluated contribution to the observed TOF mass spectra intensity for the most abundant isotope of a specific $^{28}Si_nH_x^-$ cluster, appearing at a precise $m/z$ value. In this range of H saturation, the most prominent species are the pure $Si_8^-$ cluster followed closely by the di-hydride $Si_{12}H_2^-$ species. The relative abundances have been appropriately normalized to the observed fractional intensity of $Si_8^-$.

### 3.1. $Si_8H_x^-$ ($x = 0-21$) series

The TOF spectrum of the $Si_8H_x^-$ ($x = 0-21$) mass range is displayed in Fig. 2. The most intense peak, appearing at $m/z \sim 224$ amu, is derived completely from the most abundant $^{28}Si_8^-$ isotope. Several proposed structures exist for both the neutral and anion structures, with a recent calculation pinpointing the $C_{3v}$ cage structure as the global minimum on the anion potential energy surface [36]. The adjacent peak at $m/z \sim 225$ amu is a mixture between the most abundant isotope of $^{28}Si_8H^-$ and an appreciable contribution from the second lesser isotope of $(^{28}Si_7)^{29}Si^-$. The fractional intensity of $^{28}Si_8H^-$ is determined to be the dominant component to the overall intensity of this peak, indicating single H addition does not alter the $Si_8^-$ $C_{3v}$ polyhedral structure significantly. On the contrary, the intensity contribution from $Si_8H_2^-$ ($m/z \sim 226$ amu) substantially decreases in relation to the degenerate lesser isotopes

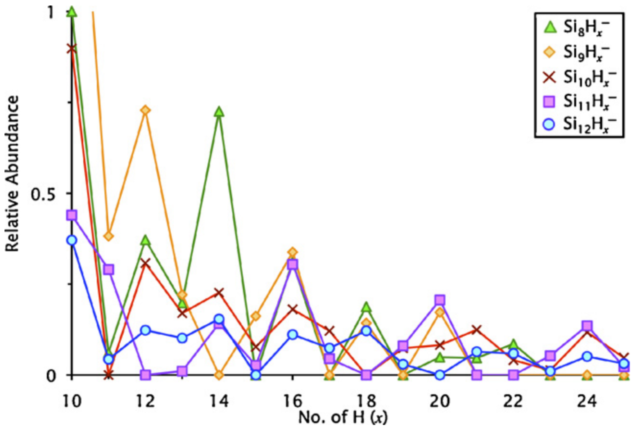

**Fig. 8.** Results of the relative abundance (*i.e.*, stability) study from the simulated isotopic distributions of the more thoroughly hydrogenated $^{28}Si_nH_x^-$ ($n = 8-12$ and $x = 10-25$) anions. Each point represents the evaluated contribution to the observed TOF mass spectra intensity for the most abundant isotope of a specific $^{28}Si_nH_x^-$ cluster, appearing at a precise $m/z$ value. The relative stability of the $Si_9H_{10}^-$ species has been shown off-scale to highlight the weaker intensity features for clusters containing H indices of $x = 16-25$. Several Si:H combinations are observed to contribute zero relative abundance to the measured intensities in the TOF spectra, and are discussed in more detail in the main text.

of $Si_8^-$ and $Si_8H^-$. This is also shown in Fig. 7, as the relative abundance of $Si_8H_2^-$ represents a minimum for the entire $Si_8H_x^-$ series. Also prevalent in Fig. 7, a pronounced even–odd alternation in cluster relative abundance, which appears to favor even H addition, begins at $Si_8H_4^-$ and ends at $Si_8H_{10}^-$. Accepting one H to $Si_8H_3^-$, an enhancement is observed for $Si_8H_4^-$, which then subsequently decreases 1 amu higher at $Si_8H_5^-$. The most abundant heavier mass cluster for the $Si_8H_x^-$ series then appears at $m/z \sim 230$ amu, corresponding to $Si_8H_6^-$. The percent abundance of the majority isotope of $^{28}Si_8H_6^-$ nearly eclipses the intensity of the dominant $^{28}Si_8H^-$ species by a small fraction. The even–odd alteration appearing in Fig. 7 suggests $Si_8H_8^-$ as another stable cluster configuration, readily comparable to the cubane analog in hydrocarbon chemistry [2]. Energetically, large amounts of strain exist in $C_8H_8$ due to the acute angles formed in the cubic structure. However, this situation may be alleviated in $Si_8H_8$ due to the natural propensity of Si to form highly compact structures that prefer 4-fold coordination and tight tetrahedral bond angles. It is interesting to note the possibility that by sequential addition of 8 H atoms, the predicted $C_{3v}$ cage structure of the parent $Si_8^-$ cluster [36] has adopted a highly symmetric $O_h$ point group at $Si_8H_8^-$.

Similar even–odd alternating trends continue in Fig. 8 for the heavier $Si_8H_x^-$, $10 \leq x \leq 21$, species. In particular, the most stable clusters, based on their relative abundances, are $Si_8H_{10}^-$, $Si_8H_{14}^-$ and $Si_8H_{18}^-$. The $Si_8H_{14}^-$ cluster, which when viewed from the hydrocarbon connectivity perspective, could be envisioned as a bicyclic structure made up of two fused 5-member pentagonal silicon rings, saturated by hydrogen atoms [2]. Analogous to the odd H containing $Si_8H_x^-$ species of Fig. 7, clusters such as $Si_8H_{11}^-$ and $Si_8H_{13}^-$ are determined to be relatively less abundant in the mass spectrum and therefore predicted to be not as stable with respect to the even hydrogen containing neighbors. Exemplifying this idea, $Si_8H_{15}^-$ and $Si_8H_{17}^-$ were determined to contribute zero intensity to the overall spectral envelope of the $Si_8H_x^-$ mass range. If any isotopic contributions of $Si_8H_{15}^-$ and $Si_8H_{17}^-$ were considered in the analysis, a substantial deviation became apparent between the experimental TOF spectrum and the fitted intensity profile. Hence, these clusters may represent totally unstable combinations of elemental Si and H, and are not present in appreciable quantities within the molecular beam.

### 3.2. $Si_9H_x$ ($x = 0$–$20$) series

Presented in Fig. 3 is the abbreviated TOF mass spectrum recorded for the $Si_9H_x^-$ ($x = 0$–$20$) mass range. The most abundant species at $m/z \sim 252$ amu is the parent anion cluster, $^{28}Si_9^-$. However, the measured signal intensity for $Si_9^-$ does not correspond to the majority peak height in the mass range of Fig. 3. Instead, the $m/z \sim 253$ amu peak possesses the greatest ion intensity due to a substantial percentage of $Si_9H^-$ being produced. The most abundant isotope of $^{28}Si_9H^-$ almost exceeds the parent $^{28}Si_9^-$ peak, attesting to the highly stable configuration of the $Si_9H^-$ cluster. Indeed, from Fig. 7, the percent abundance of $Si_9H^-$ is only slightly less than the parent $Si_9^-$ cluster. Thus, the global minimum $C_s$ structure [36] of $Si_9^-$ has not been perturbed appreciably by the addition of one hydrogen atom. Similarly noted for $Si_8H_2^-$, a decrease in relative abundance occurs when traversing from $Si_9H^-$ to $Si_9H_2^-$ via addition of one H atom. Observed in Figs. 7 and 8, a pronounced even–odd oscillation in $Si_9H_x^-$ relative abundance begins at $Si_9H_3^-$, where magic numbers correspond to odd adsorption of H to the $Si_9^-$ core, *i.e.*, $Si_9H_3^-$, $Si_9H_5^-$, $Si_9H_7^-$, and $Si_9H_9^-$, respectively.

The initial cluster abundance decline from $Si_9H^-$ to $Si_9H_2^-$ rebounds when forming the $Si_9H_3^-$ cluster. From there the even–odd alternation produces a local maximum at the $Si_9H_5^-$ mass of $m/z \sim 257$ amu. The $Si_9H_5^-$ hydride, aside from the predominant $Si_9^-$ and $Si_9H^-$ clusters, is the most abundantly produced species within this mass range. The relative stability of Fig. 7 again drops for the even H number $Si_9H_6^-$ species, and perpetuates in the oscillatory manner to $Si_9H_9^-$. For the heavily saturated $Si_9H_x^-$ ($x = 10$–$20$) species shown in Fig. 8, the $Si_9H_{10}^-$ cluster dominates in abundance for $m/z = 262$ amu. In fact, a progressive intensity rise, initiating at the $Si_9H_8^-$ isotope distribution (dark blue curve), which finally peaks at $Si_9H_{10}^-$, can be observed in the simulated isotope distributions of Fig. 3. Particularly abundant species (and therefore relatively stable) with higher indices of hydrogenation are clusters corresponding to $Si_9H_{12}^-$, $Si_9H_{16}^-$, $Si_9H_{18}^-$ and $Si_9H_{20}^-$ stoichiometries. This trend is opposite to the earlier observation deduced for the lighter $Si_9H_{3-9}^-$ hydrides from Fig. 7, where odd H numbers were observed to dominate. From the isotopic analysis of Fig. 3, zero percent abundance is determined for the even H containing cluster, $Si_9H_{14}^-$. The $Si_9H_{17}^-$ and $Si_9H_{19}^-$ hydrides were also found to possess zero abundance from the isotopic modeling. If the isotopic distributions from these species were included in the final envelope fit a significant deviation was noted from the measured TOF spectrum. This absence of mass signal may signify a highly unstable arrangement of H atoms around the $Si_9^-$ parent, which produces an extremely metastable negative ion that does not possess a sufficient lifetime to survive the $\sim$100 μs transit of the apparatus.

### 3.3. $Si_{10}H_x$ ($x = 0$–$25$) series

The results of the isotopic analysis for the $Si_{10}H_x^-$ ($x = 0$–$25$) mass range are shown in Fig. 4. The same general contour to the overall mass distribution is similar to the $Si_8H_x^-$ and $Si_9H_x^-$ profiles of Figs. 2 and 3, where the most abundant isotope is nominally the less hydrogenated cluster. This intensity trend then subsequently decays upon traversing to sufficiently higher masses where larger indices of H saturation are rampant. However, in contrast to the $Si_8H_x^-$ and $Si_9H_x^-$ mass ranges where the pure $Si_{8,9}^-$ cluster dominated the initial intensity growth, the most abundantly produced cluster for the $Si_{10}H_x^-$ mass region is the single hydrogenation product, $^{28}Si_{10}H^-$.

Discerned in Fig. 7, the $Si_{10}H^-$ cluster was the most abundantly produced species possessing one H atom with respect to the parent $Si_n^-$ cluster ($n = 8$–$12$). An equivalent intensity reduction, shown in Fig. 7, is again reverberated for the $Si_{10}H_2^-$ species, where adsorption of a single H atom to $Si_{10}H^-$ produces a significant geometric or electronic rearrangement, causing a drastic reduction in abundance and overall cluster stability. The relative abundance then increases slightly for the $Si_{10}H_3^-$ hydride. An erratic intensity profile is observed in Figs. 4 and 7 for $Si_{10}H_x^-$, signifying no clear preference of even or odd H addition. The two most abundant stoichiometries for the less saturated clusters are $Si_{10}H_6^-$ and $Si_{10}H_8^-$, with obvious decreases in stability for adjacent $Si_{10}H_7^-$ and $Si_{10}H_9^-$ clusters.

For the heavier $m/z$ hydrogenated species in Fig. 8, $Si_{10}H_{10}^-$ is evidently the most abundant isotope in that mass window. It would be of interest to ascertain whether each Si atom comprising $Si_{10}H_{10}^-$ is bonded to a single H atom, as the silicon cubane analog, $Si_8H_8^-$. Upon the addition of a single H atom to the relatively stable $Si_{10}H_{10}^-$ cluster, the isotopic modeling analysis of Fig. 4 predicts the $Si_{10}H_{11}^-$ species to be non-existent in the molecular beam, contributing zero intensity to the experimental intensity profile. A significant geometrical transition must have occurred, intuitively pointing to the simple conclusion that all “surface” bonds are quenched in $Si_{10}H_{10}^-$ and no sites are available for bonding in $Si_{10}H_{11}^-$. An abbreviated even–odd alternation then ensues past the unstable $Si_{10}H_{11}^-$ arrangement, with stable clusters evident at the even H containing moieties $Si_{10}H_{12}^-$, $Si_{10}H_{14}^-$, and $Si_{10}H_{16}^-$. As the extent of hydrogenation increases, from Figs. 4 and 8, $Si_{10}H_{18}^-$ is determined to have zero fractional intensity to the overall intensity profile. The percent abundance then increases in a stepwise manner, peaking at $Si_{10}H_{21}^-$ and $Si_{10}H_{24}^-$, respectively.

### 3.4. $Si_{11}H_x^-$ (x = 0–25) series

The results of the simulated distribution analysis for the various isotopes present in the $Si_{11}H_x^-$ ($x$ = 0–25) mass range are presented in Fig. 5. In contrast to the $Si_{8-10}H_x^-$ TOF mass spectra of Figs. 2–4, a significant departure in the general shape of the intensity contour is observed when examining the $Si_{11}H_x^-$ hydride series. Specifically, the experimental TOF spectrum of Fig. 5 peaks midway in a gaussian manner, as opposed to the exponential pattern observed earlier for the $Si_{8-10}H_x^-$ cluster distributions. This suggests that the pure $Si_{11}^-$ parent is not the most abundant cluster produced in this mass range, and likewise neither is the single hydride species, $Si_{11}H^-$. These predictions are borne out from the isotopic distribution analysis where it is observed that the most stable species, contributing majority intensity, is the $Si_{11}H_2^-$ *di*-hydride cluster, the most abundant isotope appearing at $m/z$ = 310 amu ($^{28}Si_{11}H_2^-$). Further discerned in Fig. 7, the relative abundance has a maximum at $Si_{11}H_2^-$, indicative of its energetic stability with respect to the other less saturated $Si_{11}H_x^-$ ($x$ = 0–10) hydrides. This result contrasts the previous observation made for the $Si_8H_2^-$, $Si_9H_2^-$ and $Si_{10}H_2^-$ di-hydride species, where a significant drop off in relative abundance was determined when adding one H to the more stable $Si_{8-10}H^-$ cluster.

From Figs. 5 and 7, an intensity drop in relative abundance then occurs for $Si_{11}H_3^-$. Again, this direction contradicts that observed earlier for $Si_8H_3^-$, $Si_9H_3^-$, and $Si_{10}H_3^-$ which all exhibited a definite increase in relative stability after the significant plummet of the corresponding di-hydride species. Following along this pathway of Fig. 7, another highly abundant hydride species is reached at $Si_{11}H_4^-$. The most intense peak at $m/z$ = 312 amu in the TOF mass spectrum of Fig. 5 is composed primarily of intensity contributions from the most abundant isotope of $^{28}Si_{11}H_4^-$ (along with concomitant fractional percentages of the lesser isotopes of $Si_{11}H_{0-3}^-$). A complete structural transition, originating from the neutral $Si_{11}$ spherical geometry, emerged from DFT calculations that terminated in the heavily distorted $Si_{11}H_4$ arrangement [37]. Also, unlike $Si_{11}H$, relative to the non-hydrogenated parent $Si_{11}$ cluster, $Si_{11}H_4$ was predicted to be the most energetically stable hydride species studied in the $Si_{11}H_{0-4}$ range [37].

Inspection of Fig. 8 provides insight into the relative stabilities of the larger $Si_{11}H_{10-25}^-$ negative hydride ions. Here, the $Si_{11}H_{10}^-$ cluster is identified as the most abundant species at $m/z$ = 318 amu ascertained from the simulated isotopic distributions of Fig. 5. A significant decrease in fractional intensity then commences with single H addition to form the stoichiometric $Si_{11}H_{11}^-$ species. This gradual decline in relative hydride abundance continues at $Si_{11}H_{12}^-$, which contributes zero intensity to the experimental TOF mass distribution of Fig. 5. An even–odd H fluctuation then ensues with stable hydrides being identified from Fig. 8 as $Si_{11}H_{14}^-$, $Si_{11}H_{16}^-$, $Si_{11}H_{20}^-$ and $Si_{11}H_{24}^-$, respectively. However, this alternating behavior plummets radically at $Si_{11}H_{18}^-$, $Si_{11}H_{21}^-$ and $Si_{11}H_{22}^-$, which were found to contribute zero relative abundance from the ensuing isotopic envelope fit to the TOF intensity profile. The consecutive occurrence of zero contribution from adjacent $Si_{11}H_{21}^-$ and $Si_{11}H_{22}^-$ hydrides is particularly intriguing and may signify a structural rearrangement that stabilizes only after acquiring sufficient H atoms to reach the relatively abundant $Si_{11}H_{24}^-$ structural motif.

### 3.5. $Si_{12}H_x^-$ (x = 0–25) series

The results of the isotopic distribution analysis of the $Si_{12}H_x^-$ ($x$ = 0–25) mass range are presented in Fig. 6. Again, as observed for $Si_{11}H_x^-$, the general shape of the overall experimental TOF intensity profile is radically dissimilar to that possessed by the lighter $Si_8H_x^-$, $Si_9H_x^-$, and $Si_{10}H_x^-$ hydride series. Here for $Si_{12}H_x^-$, the TOF contour shape is again reminiscent to a guassian distribution with the peak maximum centered at the midpoint of the mass spectrum, around $m/z$ = 340 amu. Thus both the pure $Si_{12}^-$ and $Si_{12}H^-$ clusters contribute only partial abundances to the overall ion intensity. The main contribution arises from the substantial production of the most abundant isotope of the $^{28}Si_{12}H_2^-$ negative cluster ion at $m/z$ = 338 amu. This trend mirrors the $Si_{11}H^- \rightarrow Si_{11}H_2^-$ transition apparent in Figs. 5 and 7. A significant increase in cluster abundance for $Si_{12}H_2^-$ is obtained when adding a single H atom to the $Si_{12}H^-$ species. This result suggests that the doubly hydrogenated species, $Si_{11}H_2^-$ and $Si_{12}H_2^-$ are especially stable clusters. The $Si_{12}H_2^-$ cluster is the second most abundant hydride detected in the current experiment for the mass range studied. Only contributions stemming from the most abundant isotope of the $^{28}Si_8^-$ cluster were present in greater intensity in the TOF mass spectrum of Fig. 1. The fractional intensity then falls for the transition $Si_{12}H_2^- \rightarrow Si_{12}H_3^-$ discerned readily in Fig. 7. Then upon sequential H addition, an appreciable abundance is determined for $Si_{12}H_4^-$, a hydride whose calculated geometry represents a deformed analog of the $Si_{12}H_3^-$ icosahedron [37]. Mimicking the trend discerned for $Si_{11}H_x^-$ in Fig. 7, after reaching an energetically favorable point in $Si_{12}H_4^-$, the relative abundance of the successively larger hydrides drops in a stepwise manner, although a slight rise is noticed at $Si_{12}H_8^-$. From Fig. 8, among the thoroughly hydrogenated series, the most abundantly produced hydride is $Si_{12}H_{10}^-$. This favorable configuration is then perturbed with single H addition in $Si_{12}H_{11}^-$, whose reduced abundance is consistent with the other eleven H containing clusters, $Si_8H_{11}^-$, $Si_9H_{11}^-$, and $Si_{10}H_{11}^-$, respectively. Also present in Fig. 8, a perceptible even–odd pattern seems to emerge at $Si_{12}H_{12}^-$ and ends sharply at $Si_{12}H_{19}^-$. Intensity contributions from the predicted isotope distributions of $Si_{12}H_{15}^-$ and $Si_{12}H_{20}^-$ were determined to be zero from the resulting isotopic envelope fit of Fig. 6. Stable clusters present in this heavier mass region are $Si_{12}H_{14}^-$, $Si_{12}H_{16}^-$ and $Si_{12}H_{18}^-$. These larger $Si_{12}H_x^-$ hydrides, possessing substantial degrees of hydrogenation, were observed to not vary significantly in relative abundance, besides a slight decline at the $Si_{12}H_{23}^-$ ion.

## 4. Conclusions

A high-resolution ($m/\Delta m \sim 400$) TOF mass spectrometric study was performed on large $Si_nH_x^-$ ($n$ = 8–12 and $0 \leq x \leq 25$) anion clusters generated from the laser-induced plasma polymerization reactions of $SiH_4$. The relative abundances of the isotopic contributions from each $Si_nH_x^-$ species, constituting the measured intensity at a precise $m/z$ value, were fully analyzed through implementation of an isotopic modeling strategy. Based on the ensuing profile fits to the TOF mass spectra, several suggestions inferring the relative stability of the hydride clusters were proposed and compared with theoretical predictions when available from the literature. The TOF spectra of the lighter mass hydride cluster anions, $Si_{8-10}H_x^-$, were dominated by contributions from the pure cluster parent, $Si_{8-10}^-$, and the single H adduct, $Si_{8-10}H^-$ species. A pronounced abrupt decrease in relative abundance was then noted for the $Si_8H_2^-$, $Si_9H_2^-$, and $Si_{10}H_2^-$ clusters. Clear even–odd alternations were observed for each cluster series, with several particularly magic species standing out amongst less abundantly produced ions. For example, in the $Si_8H_x^-$ mass range, a very stable cluster was identified at $m/z$ = 230 amu, corresponding to $Si_8H_6^-$. The probable silicon analog to the cubane stoichiometry, $Si_8H_8^-$, was also determined to be moderately abundant in the TOF spectrum.

Identified in the $Si_9H_x^-$ series was the stable $Si_9H_5^-$ cluster, which possesses the same total atom count as $Si_8H_6^-$, possibly indicating similar geometries between the separate hydrides. A transition occurred in the $Si_{10}H_x^-$ range, where the single H adduct, $Si_{10}H^-$, was determined to be more abundant than the parent $Si_{10}^-$ cluster. In the heavier cluster series investigated, $Si_{11}H_x^-$ and $Si_{12}H_x^-$, a distinct change in the overall shape of the measured TOF intensity profile was observed to shift to higher masses, rather than peak at the initial $m/z$ corresponding to the pure $Si_{11}^-$ or $Si_{12}^-$ parent. The isotopic simulations revealed the most abundant hydrides in this mass region were the di-substituted $Si_{11}H_2^-$ and $Si_{12}H_2^-$ clusters. This observation contrasted the relative abundance trends for the lighter $Si_{8-10}H_x^-$ hydrides were a substantial decrease in relative abundance was attributed to the $Si_{8-10}H_2^-$ configuration.

It has been our attempt to present experimental evidence to assist in further unraveling the myriad processes involved in the creation of dusty plasmas from the energetic discharge of $SiH_4$. Pinpointed by the employed methodology are highly stable anionic cluster motifs that represent the reactive protoparticles responsible for the initial nucleation phase. In accord with previous findings, extreme degrees of polymerization are observed for negative $Si_nH_x^-$ hydride cluster ions, further supporting their prominent role as precursors in the initial creation of microparticulate powders from reactive plasmas. We envision that the stable hydride species identified in this work could be directly incorporated in existing kinetic models involving the nucleation process, providing a more thorough description of the particle precursors and homogeneous reaction pathways the lead to powder formation. We hope these results stimulate theoretical investigations to probe the geometries and local electronic stability of these intriguing cluster systems.

## Acknowledgements

We gratefully acknowledge funding from a ARO MURI grant: W911NF-06-0280. Also, S.J.P. acknowledges J.H. Adair for suggestions regarding data analysis and J.U. Breffke for assistance in manuscript preparation and insightful discussions.

## References

[1] Ch. Hollenstein, Plasma Phys. Controlled Fusion 42 (2000) R93.
[2] M.T. Swihart, S.L. Girshick, J. Phys. Chem. B 103 (1999) 64.
[3] S.S. Talukdar, M.T. Swihart, J. Aerosol Sci. 35 (2004) 889.
[4] K. DeBleecker, A. Bogaerts, R. Gijbels, Phys. Rev. E 69 (2004) 056409.
[5] L. Ravi, S.L. Girshirk, Phys. Rev. E 79 (2009) 026408.
[6] K. DeBleecker, A. Bogaerts, W. Goedheer, R. Gijbels, IEEE Trans. Plasma Sci. 32 (2004) 691.
[7] F. Erogbogbo, K.-T. Yong, I. Roy, G. Xu, P.N. Prasad, M.T. Swihart, ACS Nano 2 (2008) 873.
[8] F. Hua, F. Erogbogbo, M.T. Swihart, E. Ruckenstein, Langmuir 22 (2006) 4363.
[9] G. Belomoin, J. Therrien, A. Smith, S. Rao, R. Twesten, S. Chaieb, M.H. Nayfeh, L. Wagner, L. Mitas, Appl. Phys. Lett. 80 (2002) 841.
[10] M.H. Nayfeh, S. Rao, N. Barry, J. Therrien, G. Belomoin, A. Smith, S. Chaieb, Appl. Phys. Lett. 80 (2002) 121.
[11] C. Courteille, J.-L. Dorier, J. Dutta, Ch. Hollenstein, A.A. Howling, T. Stoto, J. Appl. Phys. 78 (1995) 61.
[12] J. Perrin, A. Lloret, G. de Rosny, J.P.M. Schmitt, Int. J. Mass Spectrom. Ion Processes 57 (1984) 249.
[13] A. Gallagher, A.A. Howling, Ch. Hollenstein, J. Appl. Phys. 91 (2002) 5571.
[14] A.A. Howling, C. Courteille, J.-L. Dorier, L. Sansonnens, Ch. Hollenstein, Pure Appl. Chem. 68 (1996) 1017.
[15] Ch. Hollenstein, W. Schwarzenbach, A.A. Howling, C. Courteille, J.-L. Dorier, L. Sansonnens, J. Vac. Sci. Technol. A 14 (1996) 535.
[16] A.A. Howling, L. Sansonnens, J.-L. Dorier, Ch. Hollenstein, J. Appl. Phys. 75 (1994) 1340.
[17] A.A. Howling, L. Sansonnens, J.-L. Dorier, Ch. Hollestein, J. Phys. D: Appl. Phys. 26 (1993) 1003.
[18] A.A. Howling, J.-L. Dorier, Ch. Hollenstein, Appl. Phys. Lett. 62 (1993) 1341.
[19] L. Operti, R. Rabezzana, G.A. Vaglio, Rapid Commun. Mass Spectrom. 20 (2006) 2696.
[20] C. Xu, T.R. Taylor, G.R. Burton, D.M. Neumark, J. Chem. Phys. 108 (1998) 7645.
[21] C. Xu, T.R. Taylor, G.R. Burton, D.M. Neumark, J. Chem. Phys. 108 (1998) 1395.
[22] H. Murakami, T. Kanayama, Appl. Phys. Lett. 67 (1995) 2341.
[23] T.P. Martin, H. Schaber, J. Chem. Phys. 83 (1985) 855.
[24] I. Haller, Appl. Phys. Lett. 37 (1980) 282.
[25] G.A. Rechsteiner, O. Hampe, M.F. Jarrold, J. Phys. Chem. B 105 (2001) 4188.
[26] M.L. Mandich, W.D. Reents Jr., M.F. Jarrold, J. Chem. Phys. 88 (1988) 1703.
[27] M.L. Mandich, W.D. Reents Jr., J. Chem. Phys. 95 (1991) 7360.
[28] A. Melzer, in: A. Dinklage, T. Klinger, G. Marx, L. Schweikhard (Eds.), Plasma Physics: Confinement, Transport and Collective Effects, Springer, Berlin, Heidelberg, 2005.
[29] U.V. Bhandarkar, M.T. Swihart, S.L. Girshick, U.R. Kortshagen, J. Phys. D: Appl. Phys. 33 (2000) 2731.
[30] J.R. Stairs, A.W. Castleman Jr., Int. J. Mass Spectrom. 216 (2002) 75.
[31] J.R. Stairs, K.M. Davis, S.J. Peppernick, A.W. Castleman Jr., J. Chem. Phys. 119 (2003) 7857.
[32] J.R. Stairs, S.J. Peppernick, K.M. Davis, A.W. Castleman Jr., Israel J. Chem. 44 (2004) 223.
[33] K.M. Davis, S.J. Peppernick, A.W. Castleman Jr., J. Chem. Phys. 124 (2006) 164304.
[34] W.C. Wiley, I.H. McLaren, Rev. Sci. Instrum. 26 (1955) 1150.
[35] J.E. Sansonetti, W.C. Martin, J. Phys. Chem. Ref. Data 34 (2005) 1559.
[36] J.C. Yang, W.G. Xu, W.S. Xiao, J. Mol. Struct.-Theochem. 719 (2005) 89.
[37] R. Singh, J. Phys.: Condens. Matter 20 (2008) 045226.